



The effect of leading edge bluntness on scramjet performance

Tristan Vanyai^{a,*}, Nicholas N. Gibbons^a, Damian R. Curran^a, Matthew McGilvray^b,
Vincent Wheatley^a

^a School of Mechanical and Mining Engineering, The University of Queensland, St. Lucia, 4072, Australia

^b Department of Engineering Science, University of Oxford, Oxford, OX1 3PJ, United Kingdom

ARTICLE INFO

Communicated by Cummings Russell

ABSTRACT

Scramjet inlets typically ingest air that has been processed by a vehicle forebody. The forebody generates entropy and boundary layers that affect the thermodynamic properties of the ingested air and hence influence inlet mass capture, combustion performance and unstart characteristics. This paper investigates the effects of leading edge bluntness on combustion performance of a scramjet at Mach 8 flight conditions, focussing on combustion-induced pressure rise and transition between scram- and dual-mode combustion. Simulations have been performed on a 3D supersonic combustion flow path with length of order 1 m, examining the effects of forebody leading edge radii, finding that a large radius of 0.3% the engine length can produce engine unstart and significantly decrease inlet mass capture by over 45%. An experimental scramjet model has been tested to examine these effects with more reasonable, sharper radii of either 0.02% (sharp case) and 0.05% (blunt case) of the engine length for leading edges of both the forebody and the inlet walls. These experiments show that changing the forebody leading edge radii can have a strong impact on combustion mode within a scramjet flow path, with the blunt leading edge inducing dual-mode combustor earlier than the sharp leading edge. For higher equivalence ratios where both cases produce dual-mode combustion, the sharp forebody leading edge produced an increase of 5% of normalised gross thrust compared to the blunt case, indicating the increased losses for a blunt leading edge. This was consistent with numerical simulations of the two cases at an equivalence ratio of 1.4. These results suggest that changes to leading edge bluntness can influence gross thrust, engine operation mode and even trip the engine into full unstart. Thus, the leading edge radius on a hypersonic vehicle must be controlled over a vehicle's trajectory, and should not be allowed to melt or deform into a larger radius.

1. Introduction

Supersonic combustion ramjets (Scramjets) are a competitive alternative to rockets as a propulsion system for high speed atmospheric flight above Mach 5. As part of a multi-stage access-to-space system, such as the rocket-scramjet-rocket system proposed in [1], a scramjet acts as an accelerator between approximately Mach 5 to Mach 10. The primary advantages of accelerator scramjets include: Their ability to ingest incoming air, as opposed to carrying oxidizer onboard, leading to lower gross mass and increased propellant-specific impulse [2]; increased flexibility, in that they can more readily be adapted to plane-like configurations, enabling reusability, increasing launch windows and launch opportunity [3]; and decreased total fleet costs [4] and improved environmental sustainability [5] as increasing demand for satellite launches drives larger annual fleet flight rates.

A typical vehicle-integrated scramjet flow path is shown in Fig. 1, adapted from [6]. Incoming air is compressed initially by the forebody of the vehicle, and subsequently by an inlet, to pressures and temperatures suitable for combustion. Fuel is injected, typically within the combustor or upstream in the inlet, mixes with the supersonic core flow of the air and combusts, releasing heat. The combustion products are then expanded through an exhaust nozzle to generate thrust.

The defining factor of a scramjet is that the core flow through the combustor remains supersonic, thus ensuring the high total temperatures of the hypersonic freestream of the order 2500 K to 4500 K are not converted to static temperatures too high to be dealt with through common cooling methods [7]. At such high temperatures, fuel-air mixtures are not converted into final combustion products, and instead form intermediate combustion radicals through endothermic reactions, preventing the release of heat and reducing cycle efficiency. As such,

* Corresponding author.

E-mail address: t.vanyai@uq.edu.au (T. Vanyai).

<https://doi.org/10.1016/j.ast.2024.108907>

Received 13 October 2023; Received in revised form 19 December 2023; Accepted 18 January 2024

Available online 1 February 2024

1270-9638/© 2024 The Author(s). Published by Elsevier Masson SAS. This is an open access article under the CC BY-NC-ND license (<http://creativecommons.org/licenses/by-nc-nd/4.0/>).

Nomenclature

A_{nz}	Nozzle exit area	P_{ref}	Reference pressure
A_x	Area component normal to x	r	Radius
CS	Combustion-Suppressed	r_{nom}	Nominal radius
C_T	Thrust coefficient	T	Thrust
ER	Equivalence Ratio	UF	Unfuelled
M	Mach number	x	Streamwise distance
P	Pressure		

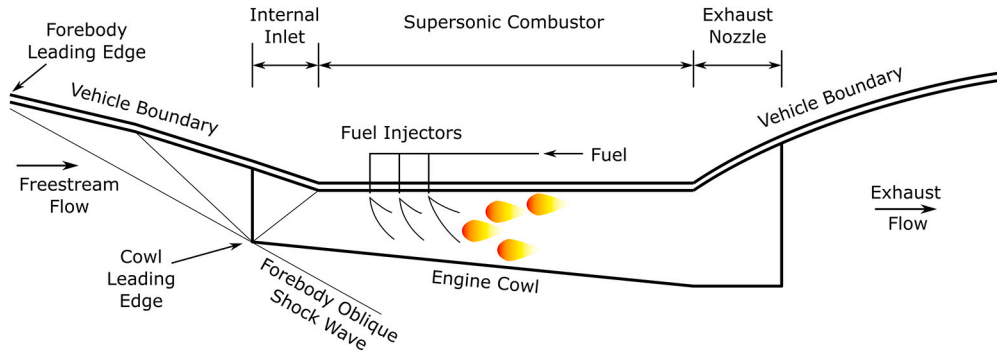


Fig. 1. Generic scramjet flow path with leading edge radii highlighted, adapted from [6].

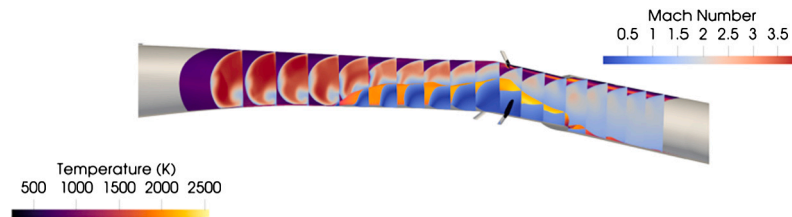


Fig. 2. Dual-mode combustion within a supersonic combustor. (For interpretation of the colours in the figure(s), the reader is referred to the web version of this article.)

a supersonic core flow becomes optimal at sufficiently high speeds, reducing the compression required of the inlet and maximising cycle efficiency [8,9]. If the flow remains predominantly supersonic throughout the combustor, this form of heat-release is termed “scram-mode combustion”. In some circumstances, e.g. [10,11], large subsonic regions can form due to boundary-layer separation around the injectors, while maintaining a supersonic core flow; this is referred to as “dual-mode combustion”.

Such a case is shown in Fig. 2 with flow from left to right, from a simulation of the flow path examined in this paper. The geometry of one symmetric half of the combustor is shown in grey, cross-section slices show Mach number, and boundary surfaces show temperature, with an iso-surface at the sonic Mach number, $M = 1$. Stoichiometric hydrogen fuel is introduced through cylindrical injectors approximately halfway along the figure, which then mixes with the core flow air and combusts. Pressure rise due to the blockage of injected fuel and subsequent combustion has caused a large separation around and upstream of the injectors on the bottom side, with temperatures of approximately 2000 K on the sonic iso-surface. The mechanism by which dual-mode combustion is initiated in this class of unobstructed flow path is documented in [12]. This separation has been able to develop upstream of the injector as the flow within this region is subsonic, however the surrounding core flow remains supersonic. As shown in [10–13], these separations can be used to increase combustor pressure and fuel residence time, resulting in improved combustion rates and combustion-induced pressure rise, even at Mach 8 [12].

Combustion within supersonic burners is currently of great interest to the research community. The transition between combustion modes is being examined in great detail, particularly for hydrocarbon fuels [10,11,14,15]. Supersonic combustion in scram- or dual-mode may be induced through the use of cavity flameholders [16–22] or even cavities in tandem [23,24]. These works are complemented by dedicated numerical studies investigating differences in chemical reaction schemes within these combustors [25,26]. Other innovative methods of improving combustion efficiencies include studies on thermal compression [27–29], flow-field manipulation via fuel injection [30], oxygen enrichment [31] or laser-induced plasma ignition [32–34].

One seemingly inconsequential geometric feature that plays a major role in hypersonic engines is the leading edge bluntness, indicated by its local radius. Increasing the radius of a leading edge can result in increased drag and changes to the entropy layer that is subsequently ingested by the scramjet engine. Historical studies have noted changes to boundary-layer transition length with increased bluntness [35,36], although it is worth noting that recent flight experiments show large variations in transition lengths from ground-based testing [37]. Studies have also examined leading edge separations in hypersonic flows [38] and flutter on wings with blunt leading edges [39]. Importantly, heat transfer at the leading edge scales inversely with the square root of the radius [40], thus sharper leading edges will lead to higher local heating rates. Uncontrolled heating loads may result in ablation or melting of the leading edge, resulting in a change of leading edge radius, in turn affecting the above flow features. The leading edge radius may potentially be preserved by active cooling methods such as transpiration

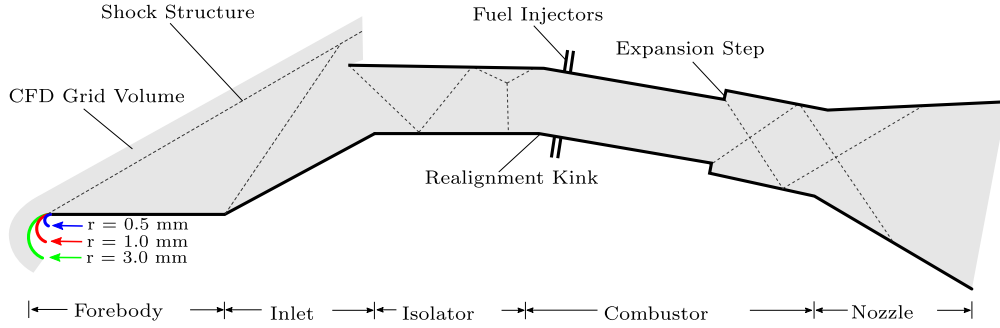


Fig. 3. 2D sketch of the CREST simulation domain, showing variants of leading edge radius. (Not to scale.)

cooling, where gas is introduced to the flow through a porous leading edge. However this gas may increase the effective leading edge radius, thus it is imperative to understand the impact downstream within a scramjet engine.

This paper examines the effects of different leading edge radii on the performance of a full scramjet engine flow path at Mach 8 flight conditions. Particular focus is placed on how leading edge bluntness affects combustion-induced pressure rise and transition between scram- and dual-mode combustion. First, numerical simulations present evidence that extreme bluntness can cause unstart due to the ingestion of large entropy layers, and suggest a reasonable limit for leading edge radii at certain scales. Second, experimental testing in a reflected shock tunnel presents results of a scramjet-like flow path with different leading edge radii and the subsequent effects on combustion modes and thrust generation potential.

2. Numerical simulations

Prior to the design of the experimental models used in this investigation, a preliminary analysis was conducted using several numerical simulations. The purpose of these simulations was to explore the range of acceptable leading edge radii and their effect on the downstream flow, particularly in the combustor. As such, the simulation geometry represents an early iteration of the design that has two minor differences compared to the final experimental model; firstly, the simulations have a slightly longer (≈ 9 mm) isolator section; and secondly, they contain an unused injector in the inlet that was not present in the final design. Neither of these changes is expected to have any important impact on the results.

Simulations were conducted using US3D, a hybrid structured/unstructured solver for general compressible flow problems, developed at the University of Minnesota [41]. US3D uses a finite-volume formulation to solve the compressible gas transport equations for the species densities, three components the momentum vector, and total energy, supplemented with an extra transport equation for the Spalart-Allmaras RANS turbulence model [42]. The governing equations solved in the present case are as follows.

$$\frac{\partial \rho_s}{\partial t} + \frac{\partial}{\partial x_j} (\rho_s u_j) + \frac{\partial}{\partial x_j} (v_{sj}) = \dot{\omega}_s \quad s = 0, \dots, n_{species} \quad (1)$$

$$\frac{\partial}{\partial t} (\rho u_i) + \frac{\partial}{\partial x_j} (\rho u_j u_i) = -\frac{\partial p}{\partial x_i} + \frac{\partial \tau_{ji}}{\partial x_j} \quad (2)$$

$$\frac{\partial}{\partial t} (E) + \frac{\partial}{\partial x_j} [(E + p)u_j] = \frac{\partial}{\partial x_j} (u_i \tau_{ji}) - \frac{\partial q_j}{\partial x_j} \quad (3)$$

$$\begin{aligned} \frac{\partial \rho \hat{v}}{\partial t} + \frac{\partial \rho \hat{v} u_j}{\partial x_j} &= \rho c_{b1} (1 - f_{t2}) \hat{S} \hat{v} - \rho \left[c_{w1} f_w - \frac{c_{b1}}{\kappa^2} f_{t2} \right] \left(\frac{\hat{v}}{d} \right)^2 \\ &+ \frac{1}{\sigma} \frac{\partial}{\partial x_j} \left(\rho (\nu + \hat{v}) \frac{\partial \hat{v}}{\partial x_j} \right) + \frac{c_{b2}}{\sigma} \rho \frac{\partial \hat{v}}{\partial x_i} \frac{\partial \hat{v}}{\partial x_i} \end{aligned} \quad (4)$$

These equations are discretised on a 3D finite-volume grid, in the present case consisting of entirely hexahedral elements, and the fluxes at each element face are computed using the Modified Steger-Warming approach discussed in [43]. Starting from an initial configuration, the flow field is advanced in time using the implicit Full-Matrix Point Relaxation (FMPR) method of [44], in which the change in conserved quantities is computed by solving a large sparse matrix problem with a data-parallel point relaxation scheme. This scheme iterates toward the solution of a linear system, by approximating the off-diagonal terms with the results from the previous iteration of the relaxation method. The simulations in this work use four iterations of FMPR to solve the linear system associated with the fluid equations, which is sufficient to achieve steady-state convergence. The equation of state is solved using the thermally perfect gas equation and the thermodynamic tables from [45], and transport properties are computed with curve fits from NASA CEA [46]. Chemical reactions are computed using the 13 species, 33 reaction hydrogen air oxidation model of [47]. This outline of the methodology is necessarily brief. More information about the numerical method can be found in [48], and the simulation details in [49].

Fig. 3 shows a sketch of the simulation geometry, sliced through the flow path symmetry plane to show the 2D structure of the flow and boundaries. The complete grid uses 22,966,744 hexahedral elements, and has been constructed in three different variants: with different forebody radii of 3 mm, 1 mm, and 0.5 mm as shown in the figure. Implicit timestepping of up to $CFL = 500$ were used to advance the simulations, which were run for 13,000, 62,500, and 74,500 steps respectively. Both the 1 mm and 0.5 mm were converged to steady-state, though the 3 mm case was unstable and unstarted, due to the extreme thickening of the entropy layer produced by the larger forebody leading edge.

Snapshots of the flow field are shown in Fig. 4, comparing the steady 1 mm case to the unsteady 3 mm case. Note the large separation visible on the body side of the inlet, which was growing as the simulation progressed. In Fig. 4, the blunt forebody leading edge (3 mm radius, or 0.3 % of the engine length) has increased the thickness of the resulting entropy layer ingested by the engine. Flow within this hot entropy layer has lower density and velocity than in the equivalent flow produced by a sharp leading edge, rendering it less able to resist flow reversal and consequent separation due to adverse pressure gradients. The shock from the cowl closure has caused the body-side boundary layer to separate in the $r = 3$ mm case. A large subsonic region has formed, significantly reducing mass flow rate through the flow path by over 45 %. It is clear that a 3 mm leading edge radius is too blunt for a scramjet-like flow path of this scale to operate as intended.

Further downstream, Fig. 5 shows pressure distributions from combustor simulations of flow paths fuelled with stoichiometric mass flow rates of hydrogen. The combustor geometry and simulation details are again documented in [50], albeit with a different fuel injector arrangement. Note that the horizontal scale in Fig. 5 has been adjusted to account for the shortening of the isolator by approximately 9 mm, so that the features in the CFD results are in the same locations as in the experimental data to be presented later. Finite-rate chemistry was

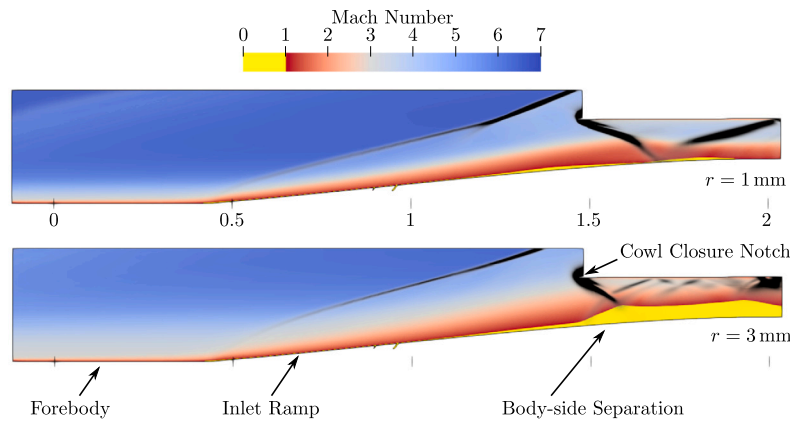


Fig. 4. Centre plane Mach number contours for 1 mm (top) and 3 mm (bottom) forebody leading edge radii. Flow is from left to right.

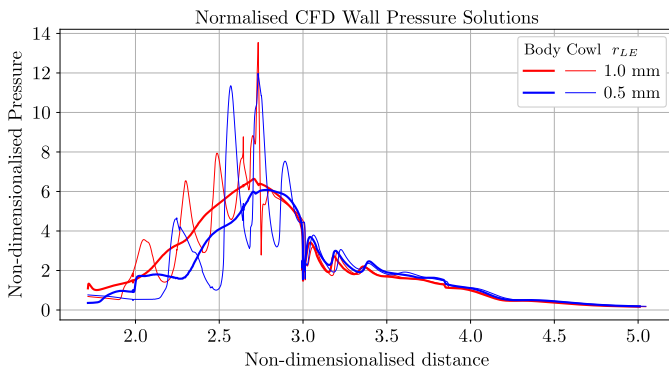


Fig. 5. Change in pressure along a fuelled scramjet flow path due to different forebody leading edge radius.

simulated using the 1992 Jachimowski 33-reaction, 13-species scheme [47]. Simulations of geometrically similar scramjet flow paths with the same chemistry scheme, turbulence modelling numerical methods, grid topology and resolution, convergence criteria and boundary conditions have been validated against experimental data for multiple combustion modes in [12].

The red, 1 mm forebody radius case in Fig. 5 shows significantly increased pressure well upstream of the injectors that propagates all the way to the inflow boundary of the combustor simulation, corresponding to the outflow of the inlet simulations of Fig. 4. This indicates that the combustor would not start for this leading edge radius, with the upstream propagation of separated flow only having been arrested by reaching the inflow boundary. As such, only a reasonably small radius of 1 mm is considered to be too blunt for testing of a flow path of order 1 m length in a practical operating mode, as these simulations indicate that the 1 mm case is prone to unstart. For the experiments in this paper, the blunt case radius was thus chosen to be 0.5 mm (where the combustor operated as intended in the simulation) and a sharp case taken as 0.2 mm to ensure manufacturability.

Note that pressure in expanding regions downstream of $x = 3.0$ is consistently higher for the 0.5 mm forebody radius case than for the 1 mm case. As such, we expect the positive inviscid thrust to be lower for blunt leading edges, due to increased total pressure losses.

3. Experimental considerations

3.1. Experimental model

An experimental model of a scramjet flow path was tested within the T4 Shock Tunnel at The University of Queensland, as shown in Fig. 6. The flow path, as described in [50], builds on the concepts of sustaining

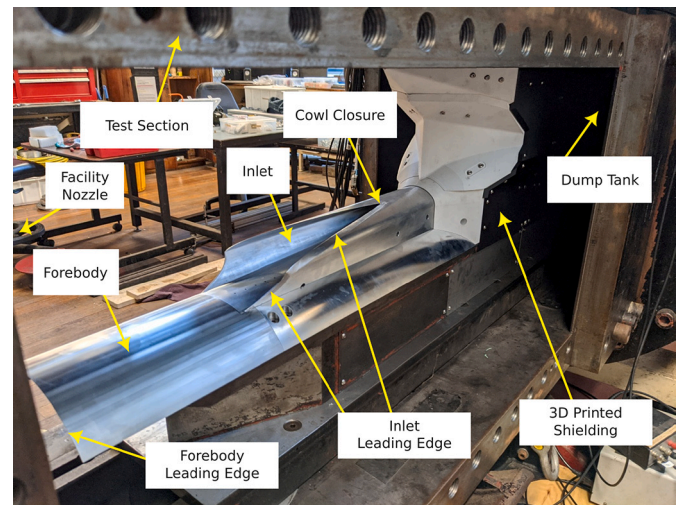


Fig. 6. Experimental test model within the T4 shock tunnel test section.

dual-mode combustion in an unobstructed combustor tested at conditions equivalent to Mach 8 flight presented previously in [12,13]. This paper examines a series of interchangeable set of inlets and forebodies with leading edge radii of 0.2 mm and 0.5 mm, or 0.02 % and 0.05 % of the engine length, respectively. Moulds were taken of the forebody leading edges and measured under a microscope, with the resulting images in Fig. 7 showing good agreement with the nominal values.

The experimental model consists of a forebody, an inlet and a constant-area isolator, followed by expanding combustor and truncated nozzle sections. Cross-sectional areas of the internal sections downstream of the inlet are shown in Fig. 8, taken relative to the nozzle exit area, with an arbitrarily normalised distance along the engine, x . The three-dimensional CREST (CRescent to Elliptical Shape Transition) inlet is shown in Fig. 6, compressing flow into the elliptical entrance of the isolator, indicated at $x = 2.4$ in Fig. 8. We define the inlet leading edge as including the upstream-facing vertical edges of the CREST inlet, the horizontal edges on the cowl-side of the CREST inlet, and the cowl closure itself, all of which had radii of either 0.2 mm or 0.5 mm. The flow becomes completely internal at the v-shaped cowl closure visible in Fig. 6, which is located at approximately $x = 1.45$. As in the previous studies, [12,51], a kink in the flow path is used to correct for the angular displacement of flow caused by the inlet, and redirect flow to the nominal flight direction. The 6° kink is located at $x = 2.65$ for this model, and is key for the combustion processes unique to this flow path. Hydrogen fuel was injected through porthole injectors at $x = 2.7$, however the model also has the capability of injection both through portholes upstream and through film injectors at $x = 3.0$. To accom-

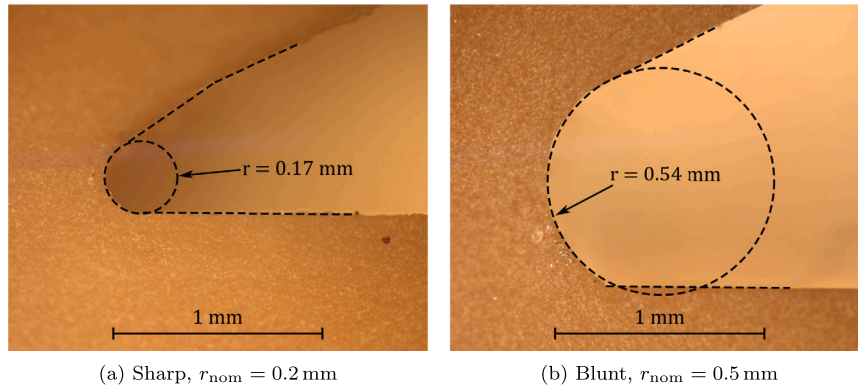


Fig. 7. Measured leading edge radii.

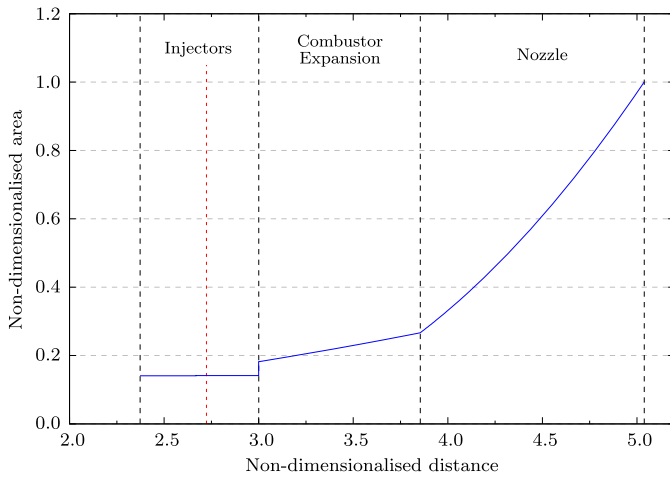


Fig. 8. Internal cross-sectional areas of the test model, downstream of the inlet.

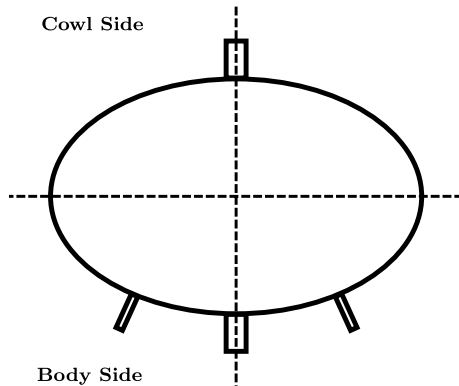


Fig. 9. Injector schematic highlighting different injector diameters.

moderate these film injectors, and to control heat release, there is a step change of area before the expanding combustor section from $x = 3.00$ to $x = 3.85$. This is followed by a final, rapid expansion through a simple, constant divergence angle nozzle from $x = 3.85$ to $x = 5.00$. The lack of an appropriately designed, large area ratio contoured thrust nozzle substantially decreases the potential for thrust generation in comparison to a realistic scramjet engine.

A key aspect of inducing dual-mode combustion in such a flow path without the highly super-stoichiometric fuelling rates required in earlier engines [12,13] is the injector layout presented in Fig. 9, which is a simplified version of that in [50]. As discussed in these previous stud-

ies, the bow shock generated by the cowl-side jet-crossflow interaction coalesces with the shock induced by the 6° bend in the flow path. This merged shock is sufficiently strong to separate the boundary layer in the wake of the large body-side injector. The shock train generated by the interaction of the crossflow may then be strong enough to generate further separations downstream. These large separations act as fluid dynamic flameholders aligned with the larger injectors located on the minor axis, whilst smaller, supplementary injectors are located off-axis in Fig. 9.

3.2. Experimental facility

Experiments were conducted in the T4 Reflected Shock Tunnel [52,53] at The University of Queensland, shown in Fig. 10. To initiate a test, a 90 kg piston is accelerated along the compression tube, driven by high pressure air from the reservoir. Argon driver gas in the compression tube is compressed in a near-isentropic manner to high pressure and temperature, bursting a 2 mm steel diaphragm located at the connection between the compression tube and the shock tube. By bursting this diaphragm, the air test gas in the shock tube is now exposed to high pressure, high temperature argon in the compression tube, producing a discontinuity and subsequent shock wave that passes down the shock tube. This shock processes the test gas, reflects off the right end of the shock tube, and reprocesses the test gas to a stagnant condition that acts as a supply reservoir for the hypersonic Mach 7 nozzle. This twice-shock-processed air bursts a secondary diaphragm (that was keeping the nozzle, test section and dump tank at vacuum) allowing flow to accelerate through the nozzle and into the test section, where the core flow is ingested into the experimental model as shown in Fig. 6. Due to the impulsive nature of this test facility and contamination from the driver gas, the test time is typically limited to the order of 1 ms.

3.3. Test condition

The inferred T4 tunnel test flow is presented in Table 1, having been calculated by taking measurements from the facility (shock speed, nozzle supply pressure, etc.) that are then processed by a state-to-state equilibrium calculator, ESTCj [54]. Similar to previous experiments [55], the test gas properties represent that of flow behind a shock produced by a hypothetical right-conical forebody with a half-angle of 5° [56] at a nominal angle of attack of 2.4° . This condition was equivalent to a vehicle at Mach 8 flight with a dynamic pressure of 45 kPa, as shown in Table 2, approximating a point on an access-to-space trajectory [8,49,57]. Conditions in Tables 1 and 2 are shown with the 95 % confidence interval of samples (i.e. $1.96 \times$ standard deviation of $n = 26$ tests); that is, the quantities fall within these ranges for 95 % of the tests conducted in this study.

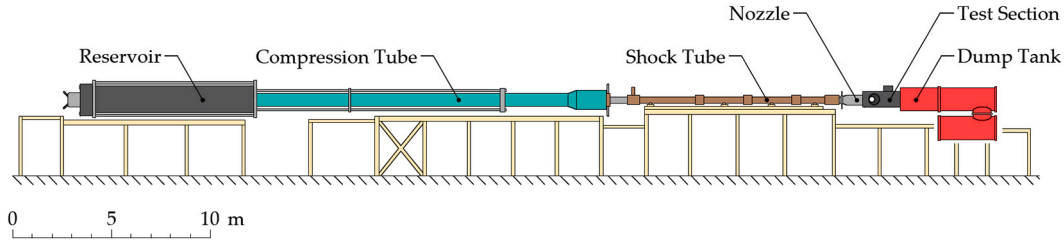


Fig. 10. T4 Shock Tunnel adapted from [51].

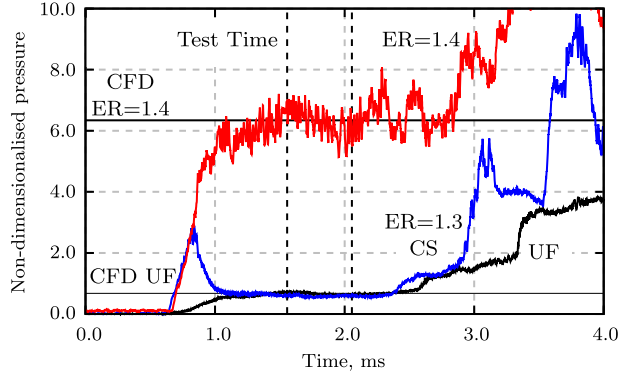
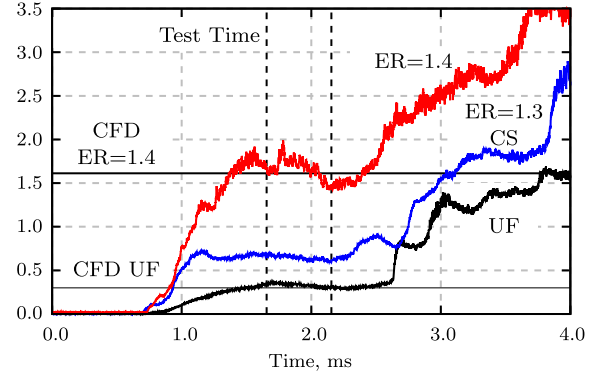
(a) Combustor Pressure at $x = 2.86$ (b) Nozzle Pressure at $x = 3.98$

Fig. 11. Variation of pressure data over test time.

Table 1

Experimental test flow, representing the conditions behind a conical forebody shock.

Quantity, units	Test condition
Mach number, –	6.88 ± 0.06
Pressure, kPa	2.22 ± 0.20
Temperature, K	302 ± 22
Density, kg m^{-3}	0.0256 ± 0.0015
Unit Reynolds number, m^{-1}	$3.26\text{e}6 \pm 0.22\text{e}6$

Table 2

Flight-equivalent freestream conditions for scramjet testing.

Quantity, units	Freestream value
Mach number, –	8.09 ± 0.21
Dynamic pressure, kPa	44.8 ± 2.8
Altitude, km	31.20 ± 0.57
Pressure, kPa	0.978 ± 0.086

3.4. Data reduction

The data presented in this paper were averaged over a test time that was adjusted according to the location of each transducer to take into account the finite travel time of a slug of test gas moving through the model, similar to the methods used previously in [58,59]. The velocity of this slug was estimated using the previous numerical simulations, with an average value of approximately 2300 m s^{-1} over the length of the model of approximately 1 m. A reference transducer was chosen near the cowl closure of the model, where the test time was first terminated due to ingestion of separated flow from the external shielding within the test section. A test time of 0.5 ms ending at the onset of this ingested flow was chosen as the test time for this transducer. The time difference was calculated for each transducer, representing the time re-

quired for the slug of test gas travelling throughout the model to reach each transducer, based on the CFD velocity. This results in time difference of the order of -0.12 ms at the inlet (upstream of the cowl closure) and $+0.28 \text{ ms}$ at the nozzle exit (downstream of the cowl closure). This process allowed for a more consistent and more representative test time selection throughout the model, whilst removing artificial variation due to the onset of the ingestion of external separated flow. The pressure traces were compared to similar experiments with external shielding removed, producing longer available test times with negligible changes to measured pressure.

Two sets of example pressure traces from the S/S experiments are shown in Fig. 11, for one pressure sensor in the combustor immediately downstream of the injectors, and one a short distance into the nozzle. Time is taken relative to the onset of pressure supply to the facility nozzle at $t = 0 \text{ ms}$. These plots show an unfuelled shot (UF), a combustion-suppressed shot (CS) and a fuelled shot with $\text{ER} = 1.4$, and compared to unfuelled (UF) and fuelled ($\text{ER} = 1.4$) CFD predictions at these locations. Note that the test time is taken slightly later for the downstream location, due to the slug-tracking method used. Throughout the test time, the transducer values are quite steady, with some added noise in the combustor case, but still with very good agreement to the CFD predictions. Variations of these pressure traces over the test time are presented later as error-bars in Section 4.

4. Experimental results

The results from experimental testing are shown in Figs. 12 to 16, presented as non-dimensionalised pressure distributions along the body side of the scramjet flow path. Equivalent pressure traces for the cowl side are given in Appendix A. The inlet compressive surfaces end approximately at non-dimensional position $x = 2.0$, followed by fuel injection indicated as a vertical dot-dash line at approximately $x = 2.7$, and finally expansion surfaces from $x = 3.0$ onward.

Experimental data from Kulite XTEL-190 series transducers are presented as discrete data points, indicating the mean pressure during the

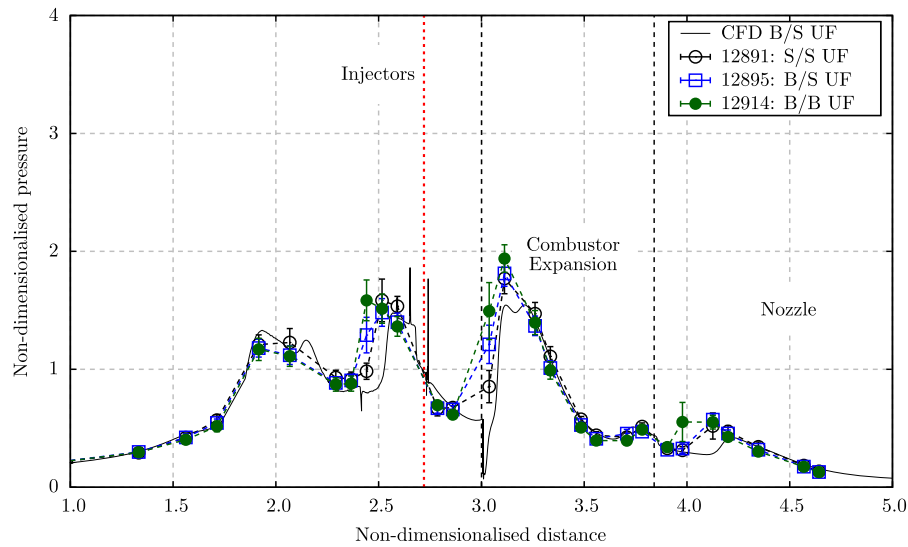


Fig. 12. Unfuelled body-side pressure distribution.

test time, with error bars representing the 95 % confidence interval of sample variation during this time. The uncertainty in these pressure measurements is typically 1 % to 3 % (or 0.1 % full-scale output) and is not included on the plots for clarity.

A legend on each plot indicates the shot reference number in the form 12XXX, being the number of test runs since T4 was first commissioned, as well as the equivalence ratio (ER) and whether the test was unfuelled (UF) or combustion-suppressed (CS) by injecting fuel into a nitrogen test gas. Experimental data are presented for the three combinations of forebody/inlet leading edges as Sharp/Sharp (S/S), Blunt/Sharp (B/S) i.e. blunt forebody and sharp inlet, and Blunt/Blunt (B/B). Note that the combustion-suppressed data for comparison to the Blunt/Sharp case are taken from the Blunt/Blunt case, as an experiment with nitrogen test was not conducted for this configuration.

For comparison, CFD simulation results are included on each plot as solid black lines for unfuelled and fully fuelled simulations. There is excellent agreement between experimental data and simulations for all cases, indicating that the operating mode of the test model and the details of the flow structure are accurately predicted by the simulations. The simulation approach was identical to that discussed in Section 2.

4.1. Unfuelled results

Examining the unfuelled pressure data in Fig. 12, the location of shocks and expansions can be identified as sudden increases and decreases in pressure, respectively. There are only minor differences in the flow structure between cases, with the later shocks shifting marginally upstream when the forebody leading edge is blunt. This is likely due to a thicker, comparatively low Mach number entropy layer being generated in this case. Aside from the minor differences in shock location, all traces agreed well with the unfuelled CFD, regardless of leading edge bluntness. As such, pressure traces from fuelled experiments will subsequently be compared against only the unfuelled, B/S CFD case to aid figure clarity.

Although not clearly visible in Fig. 12, the pressure in much of the diverging part of the combustor and the nozzle is marginally lower in the cases with blunt leading edges. This effect can be quantified by estimating the forward (axial) inviscid force on the combustor and nozzle, as described in Section 4.3. For both B/S and B/B unfuelled experiments, the integrated forward inviscid force is reduced by approximately 6% relative for the unfuelled S/S case, which is greater than experimental uncertainty (see Section 4.3). This indicates that in-

creasing leading edge bluntness may reduce the potential to generate thrust, in addition to the well known increase in drag. This will be further explored for fuelled conditions in the remaining sections.

4.2. Effect of leading edge radii and fuel equivalence ratio on operating mode

For the fuelled cases in Figs. 13 to 15, all data agree with the unfuelled CFD on the converging surfaces, both upstream and downstream of the cowl closure at approximately $x = 1.45$, until the end of the inlet. This indicates that the flow path is operating in a “started” condition for these data in the test time, where the combustion-induced pressure rise remains isolated from the inlet, minimizing pressure drag and preventing potential loss of mass capture. The unstart predicted by CFD for the combination of a large forebody leading edge radius and combustion has been successfully avoided for the leading edge radii selected for experimental testing. Downstream, within the combustor and expansion surfaces, the introduction of fuel increases pressure due to the formation of bow shocks around the injected gas, seen primarily within combustion-suppressed (CS) tests. As the fuel begins to combust, pressure increases above this CS case, indicating heat release and subsequent thrust increments on the expansion surfaces. As an example, the $ER = 1.31$ (12901) S/S test in Fig. 13 shows increased pressure rise, whilst still maintaining a clear shock-expansion train. This indicates supersonic (scram-mode) combustion.

Further increases to the fuel injection rate can lead to large subsonic separations within the combustor owing to the mechanism discussed in Section 3.1 (see [12,13]). This causes dramatic increases in pressure, even upstream of the injectors, as shown in the $ER = 1.41$ (12903) S/S test in Fig. 13. This pressure rise upstream of injection indicates the presence of large subsonic zones caused by the disruptive nature of combustion-induced pressure rise, indicating dual-mode combustion. Given the inlet remains started, with pressures remaining at unfuelled levels, this indicates the constant area isolator between the inlet and injectors is working as intended. Agreement between the experimental data and CFD confirms that flow field is dual-mode, and not completely subsonic as in ram-mode combustion.

Combustion tests were conducted for each configuration of sharp and blunt leading edges. For the sharp/sharp configuration in Fig. 13, minimal combustion-induced pressure rise was observed for the nominal $ER = 1.0$ case, and only marginal pressure increases for an $ER = 1.3$, overfuelled case. For other overfuelled cases with $ER = 1.2$ and 1.4, the experimental model transitioned into the intended dual-mode

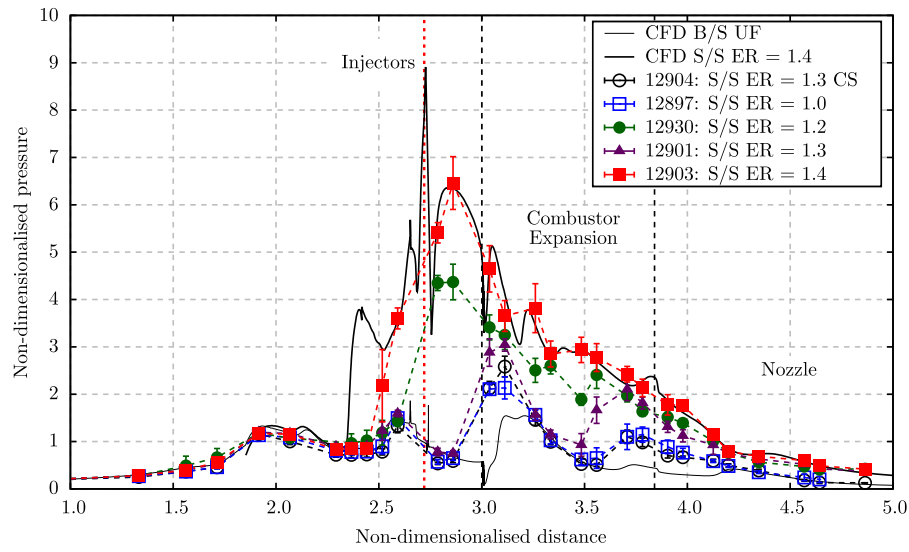


Fig. 13. Sharp/Sharp, body-side pressure distribution.

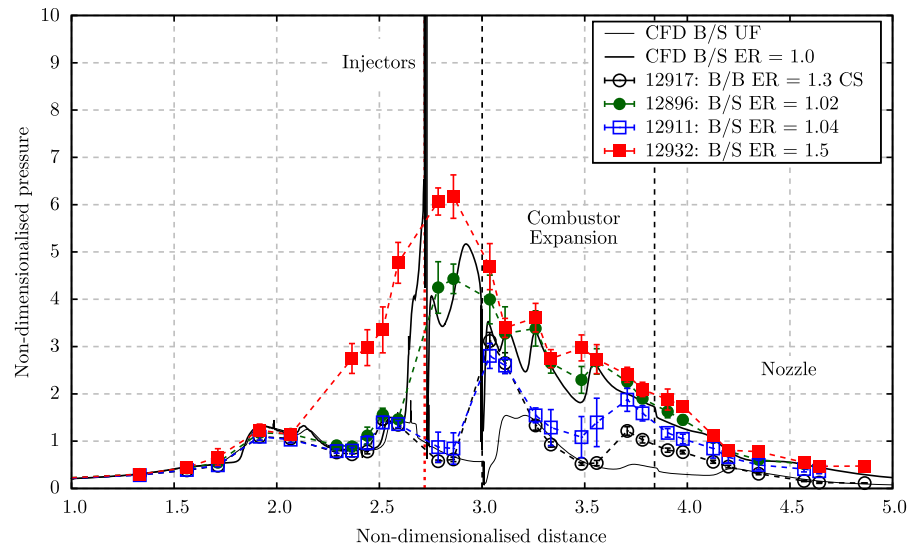


Fig. 14. Blunt/Sharp, body-side pressure distribution.

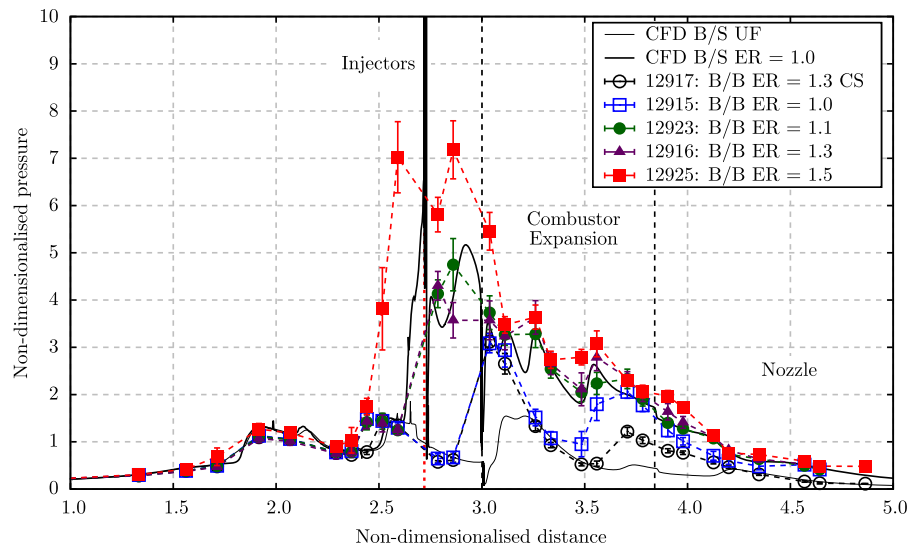


Fig. 15. Blunt/Blunt, body-side pressure distribution.

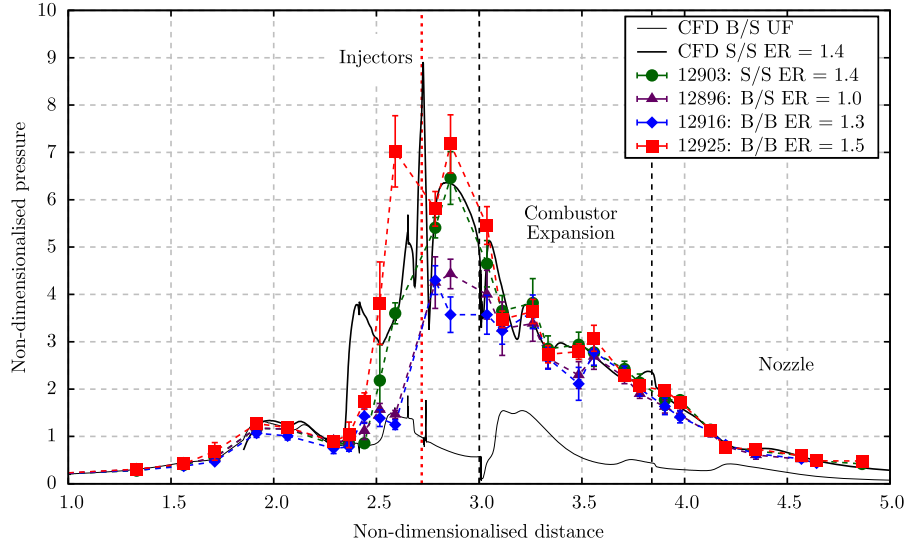


Fig. 16. Comparison between blunt and sharp forebodies, body-side pressure distribution for equivalence ratios above the transition to dual mode combustion.

combustion operating mode, with large pressure rise observed both upstream and downstream of injection. The disparity between low combustion-induced pressure rise for the $ER = 1.3$ and the dual-mode $ER = 1.2$ case is thought to be due to a combination of two factors: first, the uncertainty in equivalence ratio is approximately 11% [60], thus there may be some overlap between cases; second, the sharp/sharp case may be less conducive to dual-mode combustion at near-stoichiometric fuelling rates.

Fig. 14 shows that the lower fuelling rate limit for inducing dual-mode combustion for the blunt/sharp case is approximately stoichiometric. One $ER = 1.04$ case (12911) shows pressure values equal to the combusting CFD case (which is dual-mode) towards the rear of the model, whilst a similar fuelling rate of $ER = 1.02$ in another test (12896) shows high combustion-induced pressure rise immediately downstream of the injectors. This indicates that either combustion is dual-mode (but not spanning far enough upstream to be detected by the upstream sensors) or the fuel injection jet is acting as a flameholder, in a “jet-wake stabilized” scenario.

The blunt/blunt cases shown in Fig. 15 have a similar response to fuelling as the blunt/sharp case. The stoichiometric fuelling rate seems to be right on the border between scram-mode and dual-mode/jet-wake stabilized combustion modes. Increasing the fuelling rate further does not appear to strongly increase pressure rise towards the rear of the model, however the pressure rise has moved upstream of injection, indicating a transition to dual-mode combustion.

Collectively, the present study indicates that a greater fuelling rate, and hence stronger injector bow shocks, are required to establish dual-mode combustion for sharper leading edges. The transition equivalence ratio appears to be approximately $1.2 \pm 10\%$ for sharp leading edges and at approximately 1 when the forebody is blunt. This result is consistent with the trends observed in the inlet in Section 2, where larger leading edge radii generated a thick entropy layer that was more prone to separation.

Finally, comparison is made between blunt and sharp cases in Fig. 16. All cases shown have equivalence ratios above the relevant threshold to induce dual-mode combustion, thus the comparison shows effects of leading edge bluntness for a scramjet with consistent operating mode. The sharp/sharp dual-mode case (12903) is compared to a blunt/blunt cases with approximately 10% less fuel (12916) and 10% more fuel (12925) in terms of equivalence ratio. Due to the variable and impulsive nature of the facility, precisely matching equivalence ratios to better accuracy is difficult and was not achieved within the budgeted experiments. We note that the S/S case has comparable, if not

higher, pressures than the higher ER, B/B case (12925) within the expanding sections for positions greater than $x = 3.0$, and significantly greater pressure than the lower ER, B/B case (12916) throughout. From these trends, we conclude that at fuelling rates where the scramjet operates in dual mode, sharp leading edges result in higher pressures in the diverging sections of the geometry, which will likely result in greater thrust. These higher pressures are consistent with reduced total pressure losses in the sharp leading edge case, and indicate the disadvantage of blunter leading edges due to their higher total pressure losses.

4.3. Effect of leading edge radii on approximate combustor and nozzle inviscid thrust

To estimate the effect of leading edge radius on potential thrust, the experimentally measured pressure distributions (on both body and cowl sides) were interpolated throughout the diverging sections of the scramjet. This pressure was integrated over the streamwise-normal component of the differential wall area, i.e.

$$T = \int P \, dA_x \quad (5)$$

in the expanding combustor and nozzle sections, yielding the positive component of the inviscid thrust, T , of the model. We focus on the positive contribution to thrust of the combustor and simple nozzle since it is already well known that a blunt leading edge significantly increases the drag on the forebody and inlet. The resulting thrust values are non-dimensionalised according to

$$C_T = \frac{T}{P_{\text{ref}} A_{\text{nz}}} \quad (6)$$

where C_T is the thrust coefficient, P_{ref} is the reference pressure taken as the average of three inlet pressure transducers, and A_{nz} is the nozzle exit area.

Thrust coefficients for the S/S, B/S and B/B cases are plotted as a function of fuel equivalence ratio in Fig. 17, with key cases specified in Table 3. The uncertainty in equivalence ratio is presented as 11%, following the methodology in Appendix C of [60], and is dominated by uncertainty of the freestream air mass flux. A Monte Carlo method was used to determine the uncertainty of C_T as 2.4%. Uncertainty for each Kulite pressure transducer was taken from the manufacturer data sheet as 0.1% full-scale output, then the thrust coefficient was recalculated with a random Gaussian offset to each pressure transducer. Taking a

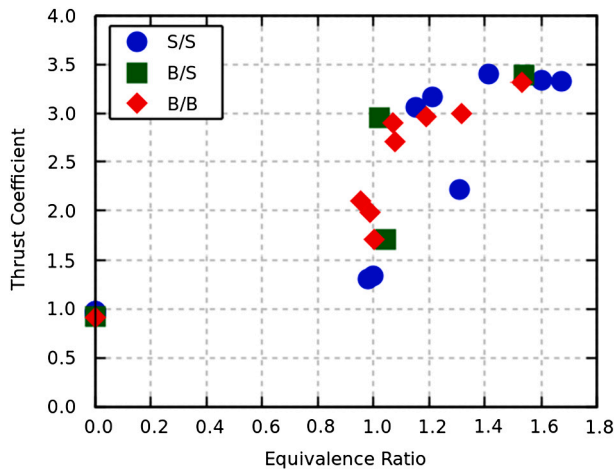


Fig. 17. Summary of thrust behaviour for all model configurations.

Table 3

Summary of thrust coefficient and combustion mode for different leading edge conditions.

Shot number	$ER \pm 11\%$	$C_T \pm 2.4\%$	Combustion mode
<i>Sharp/Sharp</i>			
12897	1.00	1.35	Minimal
12901	1.31	2.22	Scram
12930	1.15	3.11	Dual
12929	1.21	3.13	Dual
12903	1.41	3.41	Dual
<i>Blunt/Sharp</i>			
12911	1.04	1.70	Borderline Scram
12896	1.02	2.96	Dual
12932	1.54	3.33	Dual
<i>Blunt/Blunt</i>			
12926	1.00	1.70	Borderline Scram
12915	0.95	2.10	Scram
12927	1.08	2.74	Dual
12923	1.07	2.89	Dual
12918	1.19	2.96	Dual
12916	1.32	3.00	Dual
12925	1.53	3.31	Dual

large sample size of 10,000 C_T values consistently resulted in a Gaussian distribution with 95 % confidence uncertainty of 2.4 %.

Overall, the scramjet test results imply that the bluntness of a forebody leading edge may have a significant effect on scramjet performance in terms of both operating mode and thrust. Examining Fig. 17 and Table 3, the sharp forebody cases appeared to require a higher fuelling ratio to transition from scram-mode to dual-mode. Both B/S and B/B cases seemed to transition from scram-mode to dual-mode between $ER = 1.0$ to 1.1 , whilst the S/S case struggled to combust at $ER = 1.0$ and also produced scram-mode at $ER = 1.3$. A later test did show dual-mode combustion for a S/S case at $ER = 1.2$, so the transition from scram- to dual-mode may be approximately $ER = 1.2$ to 1.3 , which can be explained by the 11 % uncertainty in equivalence ratio.

For large equivalence ratios where all engine variants operate in dual-mode, the trend is for the sharp leading edge model to produce greater gross thrust. For example, for Shot 12930 S/S $ER = 1.15$, $C_T = 3.13$ compared with $C_T = 2.96$ (−5.4%) for the B/B case of Shot 12918, $ER = 1.19$. Given the uncertainty of 2.4 %, this results in an increase in thrust coefficient of $\Delta C_T = 0.17 \pm 0.10$, with more than 99.9 % confidence that the S/S has a greater thrust coefficient than the B/B case. This implies that there are greater total pressure losses in the blunt cases. This increase in C_T was confirmed with numerical simulations of Shot 12903, a S/S case with $ER = 1.4$. When the sharp leading edge of

the forebody was changed to blunt, from $r = 0.2$ mm to $r = 0.5$ mm (or 0.02 % and 0.05 % of the engine length, respectively) the inviscid thrust in the expanding sections decreased by 5.2 %. At larger, more significantly overfuelled cases around $ER = 1.6$, this trend seems to go away as the thrust coefficient plateaus for all leading edge cases.

The leading edge radii of the forebody and inlet should thus be known and controlled precisely to ensure scramjets operate in the intended combustion mode whilst maximizing thrust.

5. Conclusions

The effects of leading edge bluntness on scramjet performance have been examined numerically and experimentally. Simulations show that for a 1 m scale scramjet flow path, increasing the forebody leading edge radius from 0.5 mm to 3.0 mm (from 0.05 % to 0.3 % of the engine length) reduces the mass capture of air by over 45 %, and can cause unstart. Leading edges at this scale are therefore limited to approximately 0.5 mm (0.05 % engine length), which informed the design of the experimental model tested in the T4 reflected shock tunnel.

Experimental tests of a scramjet with forebody and inlet leading edges of 0.2 mm and 0.5 mm radius (0.02 % and 0.05 % of the engine length, respectively) referred to as the sharp and blunt leading edges, show that leading edge bluntness can change combustion considerably, with changeover between scram-mode and dual-mode occurring at significantly higher equivalence ratios for the sharp case. The S/S case did not exhibit dual-mode combustion until $ER = 1.15$, with a scram-mode case occurring at $ER = 1.31$, whilst the B/S and B/B cases had dual-mode cases as low as $ER = 1.02$ and $ER = 1.07$ respectively.

All configurations do exhibit scram- and dual-mode combustion at certain operating points within the range of equivalence ratios tested. At near-stoichiometric fuelling rates where both leading edge radii resulted in dual-mode combustion, greater pressures were observed in the diverging, thrust producing sections of the flow path for the sharp leading edge case compared with the blunt forebody cases. This resulted in increased thrust coefficients of $C_T = 3.11$ for the S/S case at $ER = 1.12$, compared to 2.96 and 3.00 for B/B cases of $ER = 1.19$ and $ER = 1.32$ respectively. At this flight condition of Mach 8, 44.8 kPa dynamic pressure, dual-mode combustion has resulted in significantly larger thrust coefficients over scram-mode combustion, of the order 30 % to 40 % with only minor changes in fuelling. We infer that sharper forebody leading edges (of radius approximately 0.2 % of the total engine length) produce lower total pressure losses, and are preferred in the case where dual-mode combustion and appropriate cooling can be ensured.

For scramjet flow paths of the type studied here, the above evidence points to tight control of forebody leading edge radii being required: radii smaller than the design point may prevent the establishment of the intended combustion mode, while significantly blunter than designed radii lead to increased total pressure losses and decreased thrust, decreased mass capture and, in the extreme computational case studied, engine unstart.

CRedit authorship contribution statement

Tristan Vanyai: Conceptualization, Data curation, Formal analysis, Investigation, Methodology, Validation, Visualization, Writing – original draft, Writing – review & editing. **Nicholas N. Gibbons:** Conceptualization, Data curation, Formal analysis, Investigation, Methodology, Validation, Visualization, Writing – original draft, Writing – review & editing. **Damian R. Curran:** Conceptualization, Data curation, Formal analysis, Investigation, Methodology, Visualization. **Matthew McGilvray:** Conceptualization, Funding acquisition, Project administration, Resources, Supervision, Writing – review & editing. **Vincent Wheatley:** Conceptualization, Funding acquisition, Investigation, Project administration, Resources, Supervision, Writing – review & editing.

Declaration of competing interest

The authors declare the following financial interests/personal relationships which may be considered as potential competing interests: Matthew McGilvray reports financial support was provided by Defense Advanced Research Projects Agency. If there are other authors, they declare that they have no known competing financial interests or personal relationships that could have appeared to influence the work reported in this paper.

Data availability

The authors do not have permission to share data.

Acknowledgements

The authors thank the T4 Team: Jacob Sandral, Ramprakash Ananthapadmanaban, Keill Hopkins, Hugh Russell, Oliver Street, Matthew

Thompson, Matthew Trudgian and Keith Hitchcock; as well as Michael K. Smart and Ryan Whitside for discussions and initial contributions to this project. This project is funded through “Transpiration Cooling to Enable Sharp Leading Edge Technology” in response to DARPA call HR001119S0022 “MACH - Materials Architectures and Characterization for Hypersonics”. The views, opinions and/or findings expressed are those of the author and should not be interpreted as representing the official views or policies of the Department of Defense or the U.S. Government. This paper has been approved for release by DARPA under Distribution Statement “A” (Approved for Public Release, Distribution Unlimited). This research was undertaken with the assistance of resources and services from the National Computational Infrastructure (NCI), which is supported by the Australian Government.

Appendix A. Cowl-side pressure traces

The cowl pressure traces corresponding to Figs. 12 to 16 are presented in this appendix as Figs. A.1 to A.5.

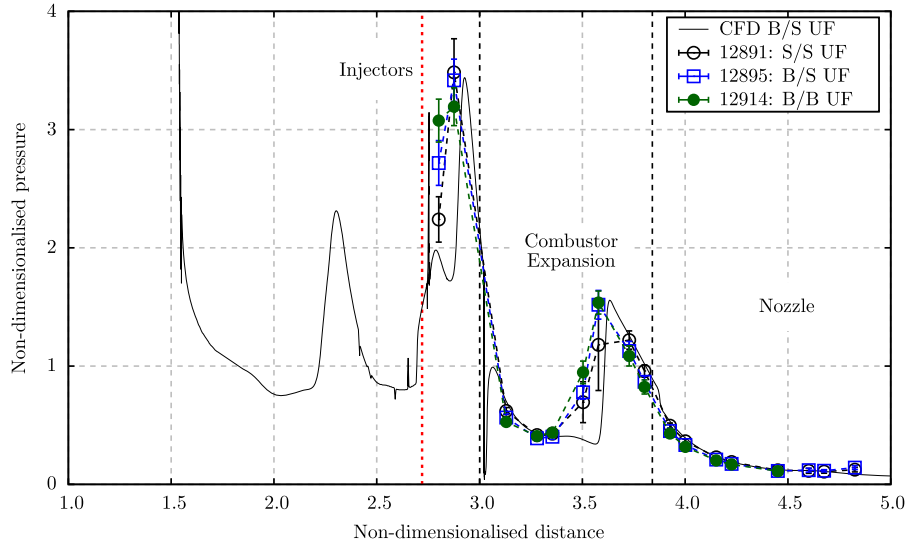


Fig. A.1. Unfuelled cowl-side pressure distribution.

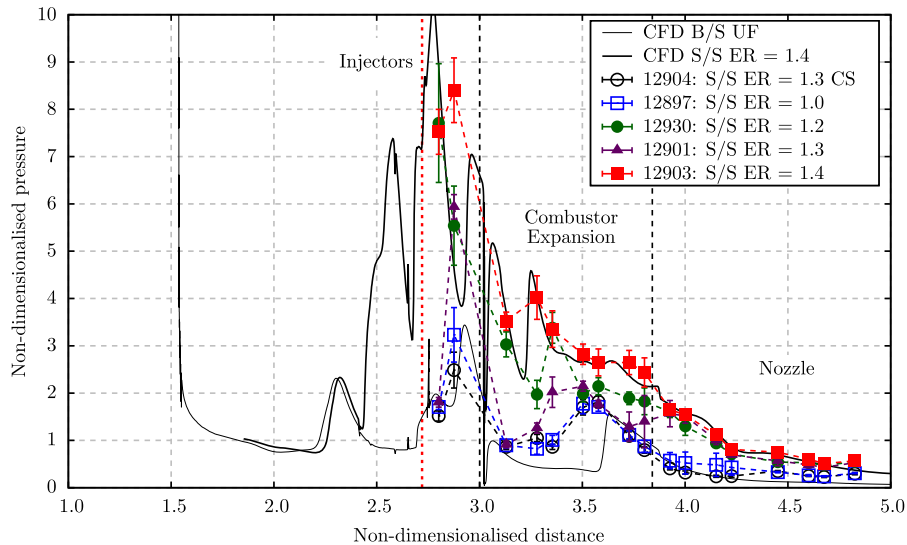


Fig. A.2. Sharp/Sharp, cowl-side pressure distribution.

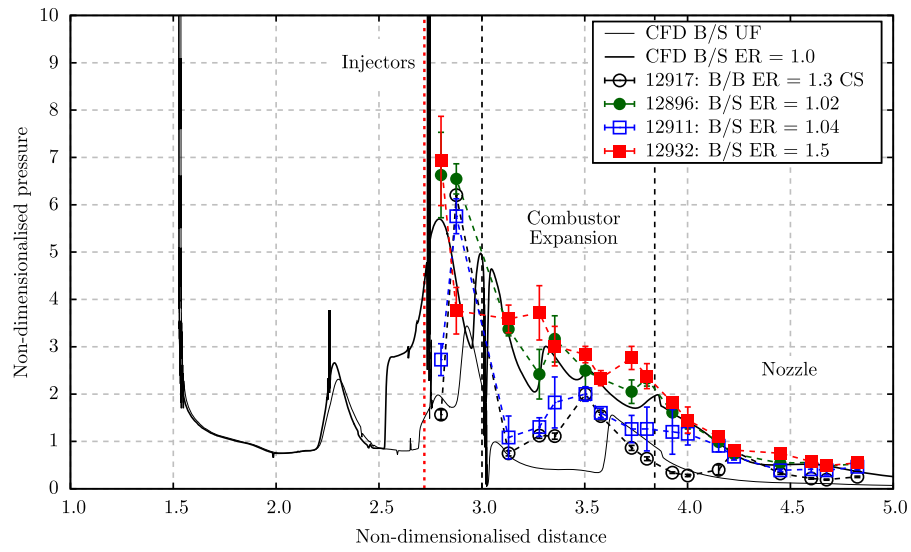


Fig. A.3. Blunt/Sharp, cowl-side pressure distribution.

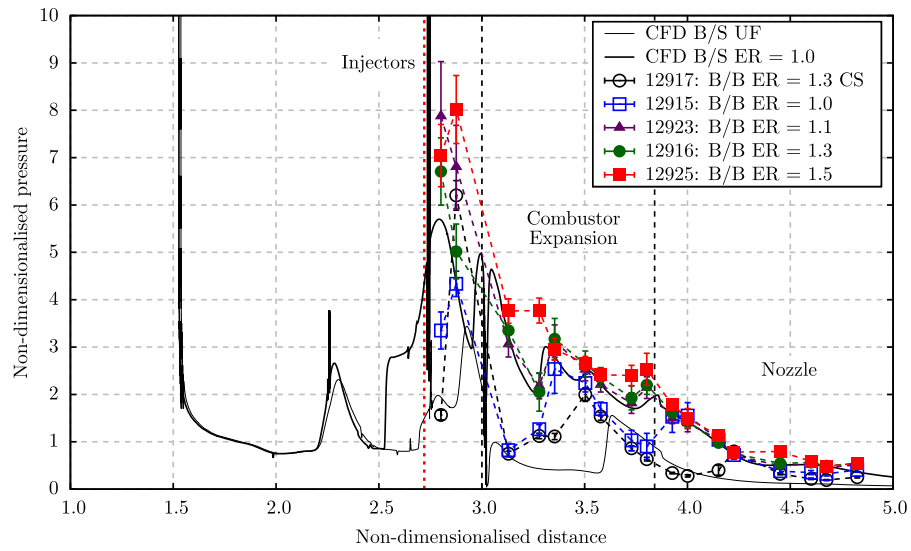


Fig. A.4. Blunt/Blunt, cowl-side pressure distribution.

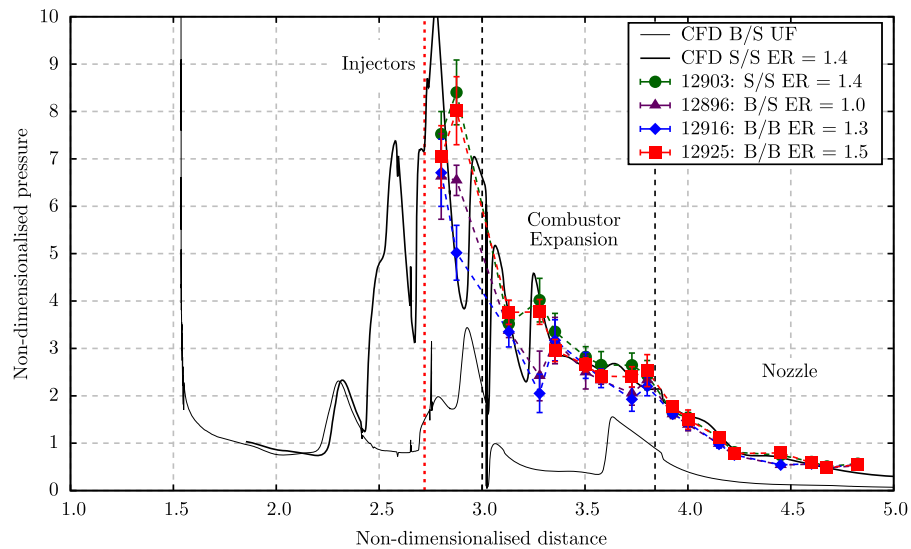


Fig. A.5. Comparison between blunt and sharp forebodies, cowl-side pressure distribution.

References

- [1] M.K. Smart, M.R. Tetlow, Orbital delivery of small payloads using hypersonic air-breathing propulsion, *J. Spacecr. Rockets* 46 (1) (2009) 117–125, <https://doi.org/10.2514/1.38784>.
- [2] D.L. Kors, Design considerations for combined air breathing-rocket propulsion systems, in: *AIAA Second International Aerospace Planes Conference*, AIAA, United States, 1990.
- [3] K.W. Flaherty, K.M. Andrews, G.W. Liston, Operability benefits of airbreathing hypersonic propulsion for flexible access to space, *J. Spacecr. Rockets* 47 (2) (2010) 280–287, <https://doi.org/10.2514/1.43750>.
- [4] K. Bowcutt, M. Gonda, T. Ralston III, S. Hollowell, Performance, economic, and operational drivers of reusable launch vehicles, in: *38th AIAA/ASME/SAE/ASEE Joint Propulsion Conference & Exhibit*, 2002, p. 3901.
- [5] L.M. McTaggart, T. Vanyai, M.K. Smart, Commercial potential evaluation of scramjet powered vehicles for access-to-space, in: *AIAA SCITECH 2023 Forum*, 2023, p. 2685.
- [6] W.H. Heiser, D.T. Pratt, *Hypersonic Airbreathing Propulsion*, AIAA, 1994.
- [7] A. Ferri, Mixing-controlled supersonic combustion, *Annu. Rev. Fluid Mech.* 5 (1973) 301–338, <https://doi.org/10.1146/annurev.fl.05.010173.001505>.
- [8] M.K. Smart, How much compression should a scramjet inlet do?, *AIAA J.* 50 (3) (2012) 610–619, <https://doi.org/10.2514/1.J051281>.
- [9] T. Vanyai, M. Bricalli, S. Brieschenk, R.R. Boyce, Scramjet performance for ideal combustion processes, *Aerosp. Sci. Technol.* 75 (2018) 215–226, <https://doi.org/10.1016/j.ast.2017.12.021>.
- [10] T. Vanyai, W.O. Landsberg, T.J. McIntyre, A. Veeraragavan, OH visualization of ethylene combustion modes in the exhaust of a fundamental, supersonic combustor, *Combust. Flame* 226 (2021) 143–155, <https://doi.org/10.1016/j.combustflame.2020.11.037>.
- [11] W.O. Landsberg, T. Vanyai, T.J. McIntyre, A. Veeraragavan, Dual/scram-mode combustion limits of ethylene and surrogate endothermically-cracked hydrocarbon fuels at Mach 8 equivalent high-enthalpy conditions, *Proc. Combust. Inst.* 38 (3) (2021) 3835–3843, <https://doi.org/10.1016/j.proci.2020.07.003>.
- [12] D. Curran, V. Wheatley, M. Smart, Investigation of combustion mode control in a Mach 8 shape-transitioning scramjet, *AIAA J.* 57 (7) (2019) 2977–2988, <https://doi.org/10.2514/1.J057999>.
- [13] J.C. Turner, M.K. Smart, Mode change characteristics of a three-dimensional scramjet at Mach 8, *J. Propuls. Power* 29 (4) (2013) 982–990, <https://doi.org/10.2514/1.B34569>.
- [14] M. Ravindran, M. Bricalli, A. Pudsey, H. Ogawa, Mixing characteristics of cracked gaseous hydrocarbon fuels in a scramjet combustor, *Acta Astronaut.* 162 (2019) 168–184, <https://doi.org/10.1016/j.actaastro.2019.06.010>.
- [15] W. Shen, Y. Huang, Y. You, L. Yi, Characteristics of reaction zone in a dual-mode scramjet combustor during mode transitions, *Aerosp. Sci. Technol.* 99 (2020) 105779, <https://doi.org/10.1016/j.ast.2020.105779>.
- [16] Z.J. Denman, W.Y.K. Chan, S. Brieschenk, A. Veeraragavan, V. Wheatley, M.K. Smart, Ignition experiments of hydrocarbons in a Mach 8 shape-transitioning scramjet engine, *J. Propuls. Power* 32 (6) (2016) 1462–1471, <https://doi.org/10.2514/1.B36099>.
- [17] T. Vanyai, S. Grieve, O. Street, Z. Denman, T. McIntyre, A. Veeraragavan, V. Wheatley, M. Smart, Fundamental scramjet combustion experiments using hydrocarbon fuel, *J. Propuls. Power* 35 (5) (2019) 953–963, <https://doi.org/10.2514/1.B37472>.
- [18] Q. Liu, D. Baccarella, W. Landsberg, A. Veeraragavan, T. Lee, Cavity flameholding in an optical axisymmetric scramjet in Mach 4.5 flows, *Proc. Combust. Inst.* 37 (3) (2019) 3733–3740, <https://doi.org/10.1016/j.proci.2018.08.037>.
- [19] E. Jeong, S. O'Byrne, I.-S. Jeung, A.F.P. Houwing, The effect of fuel injection location on supersonic hydrogen combustion in a cavity-based model scramjet combustor, *Energies* 13 (1) (2020), <https://doi.org/10.3390/en13010193>.
- [20] M.A. Trudgian, W.O. Landsberg, A. Veeraragavan, Experimental investigation of inclining the upstream wall of a scramjet cavity, *Aerosp. Sci. Technol.* 99 (2020) 105767, <https://doi.org/10.1016/j.ast.2020.105767>.
- [21] T. Roos, A. Pudsey, H. Ogawa, Numerical investigation of combustion characteristics of upstream crescent cavities in a scramjet combustor, *Acta Astronaut.* 187 (2021) 43–60, <https://doi.org/10.1016/j.actaastro.2021.05.027>.
- [22] P. Xiong, D. Zheng, Y. Tan, Y. Tian, J. Le, Experimental study of ignition and combustion characteristics of ethylene in cavity-based supersonic combustor at low stagnation temperature and pressure, *Aerosp. Sci. Technol.* 109 (2021) 106414, <https://doi.org/10.1016/j.ast.2020.106414>.
- [23] Y. hang Wang, W. yan Song, D. yong Shi, Investigation of flameholding characteristics in a kerosene-fueled scramjet combustor with tandem dual-cavity, *Acta Astronaut.* 140 (2017) 126–132, <https://doi.org/10.1016/j.actaastro.2017.08.014>.
- [24] S.A. Mecklem, W.O. Landsberg, D. Curran, A. Veeraragavan, Combustion enhancement via tandem cavities within a Mach 8 scramjet combustor, *Aerosp. Sci. Technol.* 124 (2022) 107551, <https://doi.org/10.1016/j.ast.2022.107551>.
- [25] K. Kannaiyan, Numerical investigation of the local and global supersonic combustion characteristics of ethylene fuel, *Aerosp. Sci. Technol.* 106 (2020) 106178, <https://doi.org/10.1016/j.ast.2020.106178>.
- [26] N. Gibbons, T. Vanyai, V. Wheatley, Comparison of ethylene combustion mechanisms for the simulation of a supersonic combustion experiment, *Aerosp. Sci. Technol.* 119 (2021) 107201, <https://doi.org/10.1016/j.ast.2021.107201>.
- [27] M.G. Bricalli, L.M. Brown, R.R. Boyce, Numerical investigation into the combustion behavior of an inlet-fueled thermal-compression-like scramjet, *AIAA J.* 53 (7) (2015) 1740–1760, <https://doi.org/10.2514/1.J053513>.
- [28] M.G. Bricalli, L. Brown, R.R. Boyce, R. Gollan, T. Vanyai, A.S. Pudsey, Scramjet performance with nonuniform flow and swept nozzles, *AIAA J.* 56 (10) (2018) 3988–4003, <https://doi.org/10.2514/1.J056963>.
- [29] T. Vanyai, S. Brieschenk, M. Bricalli, T. Sopek, T.J. McIntyre, Thermal compression effects within a fundamental, hydrogen-fueled scramjet, *Aerosp. Sci. Technol.* 110 (2021) 106499, <https://doi.org/10.1016/j.ast.2021.106499>.
- [30] W.O. Landsberg, N.N. Gibbons, V. Wheatley, M.K. Smart, A. Veeraragavan, Improving scramjet performance through flow field manipulation, *J. Propuls. Power* 34 (3) (2018) 578–590, <https://doi.org/10.2514/1.B36772>.
- [31] A.F. Moura, N. Gibbons, V. Wheatley, I. Jahn, Effects of oxygen enrichment on supersonic combustion in a Mach 10 scramjet, *AIAA J.* 59 (11) (2021) 4556–4568, <https://doi.org/10.2514/1.J059748>.
- [32] S. Brieschenk, S. O'Byrne, H. Kleine, Ignition characteristics of laser-ionized fuel injected into a hypersonic crossflow, *Combust. Flame* 161 (4) (2014) 1015–1025, <https://doi.org/10.1016/j.combustflame.2013.09.024>.
- [33] N. Gibbons, R. Gehre, S. Brieschenk, V. Wheatley, Simulation of laser-induced plasma ignition in a hypersonic crossflow, *AIAA J.* 56 (8) (2018) 3047–3059, <https://doi.org/10.2514/1.J055821>.
- [34] D. Baccarella, G.-S. Lee, Q. Liu, G.S. Elliott, J. Freund, T. Lee, Laser-induced plasma ignition experiments in a direct-connect supersonic combustor at Mach 3, in: *AIAA Propulsion and Energy 2019 Forum*, 2019.
- [35] D. Jillie, E. Hopkins, Effects of Mach number, leading-edge bluntness, and sweep on boundary-layer transition, *Tech. Rep. TN D-1071*, NASA, 1961.
- [36] S. Mallinson, S. Gai, N. Mudford, Leading-edge bluntness effects in high enthalpy, hypersonic compression corner flow, *AIAA J.* 34 (11) (1996) 2284–2290, <https://doi.org/10.2514/3.13392>.
- [37] R.L. Kimmel, D.W. Adamczak, D. Hartley, H. Alesi, M.A. Frost, R. Pietsch, J. Shannon, T. Silvester, Hypersonic international flight research experimentation-5b flight overview, *J. Spacecr. Rockets* 55 (6) (2018) 1303–1314, <https://doi.org/10.2514/1.A34148>.
- [38] L.M. Le Page, M. Barrett, S. O'Byrne, S.L. Gai, Laser-induced fluorescence velocimetry for a hypersonic leading-edge separation, *Phys. Fluids* 32 (3) (2020) 036103, <https://doi.org/10.1063/5.0004266>.
- [39] C. Ji, W. Jiang, J. Zhu, Z. Liu, F. Li, Experimental study of hypersonic flutter of a blunt-leading-edge trapezoidal wing, in: *21st AIAA International Space Planes and Hypersonics Technologies Conference*, 2017.
- [40] K. Sutton, R.A. Graves Jr, A general stagnation-point convective heating equation for arbitrary gas mixtures, *Tech. Rep. NASA-TR-R-376*, NASA, 1971.
- [41] G.V. Candler, H.B. Johnson, I. Nompelis, P.K. Subbareddy, T.W. Drayna, V. Gidzak, Development of the us3d code for advanced compressible and reacting flow simulations, in: *53rd AIAA Aerospace Sciences Meeting*, No. 2015-1893, Kissimmee, Florida, 2015.
- [42] S.R. Allmaras, F.T. Johnson, P. Spalart, Modifications and clarifications for the implementation of the Spalart-Allmaras turbulence model, in: *Seventh International Conference on Computational Fluid Dynamics*, Big Island, Hawaii, 2012.
- [43] I. Nompelis, T. Drayna, G. Candler, Development of a hybrid unstructured implicit solver for the simulation of reacting flows over complex geometries, in: *34th AIAA Fluid Dynamics Conference and Exhibit*, 2004, p. 2227.
- [44] M. Wright, G. Candler, M. Prampolini, Data-parallel lower-upper relaxation method for the Navier-Stokes equations, *AIAA J.* 34 (7) (1996) 1371–1377.
- [45] B.J. McBride, M.J. Zehe, S. Gordon, Nasa Glenn coefficients for calculating thermodynamic properties of individual species, *Tech. Rep. 211556*, National Aeronautics and Space Administration, 2002.
- [46] S. Gordon, B.J. McBride, Computer program for calculation of complex chemical equilibrium compositions and applications, *Tech. Rep. Reference Publication 1311*, National Aeronautics and Space Administration, 1994.
- [47] C.J. Jachimowski, An analysis of combustion studies in shock expansion tunnels and reflected shock tunnels, *Tech. Rep. NASA-TP-3224*, NASA, 1992.
- [48] N.N. Gibbons, Simulation and dynamics of hypersonic combustion, Ph.D. thesis, the University of Queensland, School of Mechanical and Mining Engineering, St Lucia, QLD 4072, 2019.
- [49] D. Curran, V. Wheatley, M. Smart, High Mach number operation of accelerator scramjet engine, *J. Spacecr. Rockets* (2022) 1–15, <https://doi.org/10.2514/1.A35511>.
- [50] D. Curran, V. Wheatley, M. Smart, The effect of wall and fuel temperature in a Mach 6 scramjet engine, in: *22nd Australasian Fluid Mechanics Conference AFMC2020*, No. 219, The University of Queensland, 2020.
- [51] L.J. Doherty, An experimental investigation of an airframe integrated three-dimensional scramjet engine at a Mach 10 flight condition, PhD Thesis, The University of Queensland, Australia, 2014.
- [52] R.J. Stalker, A study of the free-piston shock tunnel, *AIAA J.* 5 (12) (1967) 2160–2165, <https://doi.org/10.2514/3.4402>.
- [53] R. Stalker, R. Morgan, The University of Queensland free piston shock tunnel T4 - initial operation and preliminary calibration, in: *Fourth National Space Engineering Symposium*, Institution of Engineers, Australia, 1988, pp. 182–198.
- [54] P. Jacobs, A. Gardner, K. Hannemann, Gas-dynamic modelling of the HEG shock tunnel, DLR-IB 224-2003 A02, Deutsches Zentrum für Luft- und Raumfahrt E.V., 2003.

- [55] R.W. Whitside, M.K. Smart, Low Mach number testing of a scramjet for access to space, in: 23rd AIAA International Space Planes and Hypersonic Systems and Technologies Conference, 2020.
- [56] D. Preller, M.K. Smart, Reusable launch of small satellites using scramjets, *J. Spacecr. Rockets* 54 (6) (2017) 1317–1329, <https://doi.org/10.2514/1.A33610>.
- [57] S.O. Forbes-Spyratos, M.P. Kearney, M.K. Smart, I.H. Jahn, Trajectory design of a rocket–scramjet–rocket multistage launch system, *J. Spacecr. Rockets* 56 (1) (2019) 53–67, <https://doi.org/10.2514/1.A34107>.
- [58] M. McGilvray, R.G. Morgan, P.A. Jacobs, Scramjet experiments in an expansion tunnel: evaluated using a quasi-steady analysis technique, *AIAA J.* 48 (8) (2010) 1635–1646.
- [59] M. McGilvray, R. Kirchhartz, T. Jazra, Comparison of Mach 10 scramjet measurements from different impulse facilities, *AIAA J.* 48 (8) (2010) 1647–1651.
- [60] T. Vanyai, Experimental investigation of a 3D thermal compression scramjet using advanced optical techniques, PhD Thesis, The University of Queensland, Australia, 2018.